Original Article

Spatial position changes in the semicircular canals may be the anatomical basis of Meniere's disease: a preliminary study based on ultra-high-resolution computed tomography (CT) and intelligent segmentation

Yan Huang[1]^, Ke Liu[2]^, Ruowei Tang[1]^, Ning Xu[1]^, Jing Xie[3]^, Zhenghan Yang[1]^, Hongxia Yin[1]^, Xiaoguang Li[2]^, Zhenchang Wang[1]^, Pengfei Zhao[1]^

[1]Department of Radiology, Beijing Friendship Hospital, Capital Medical University, Beijing, China; [2]School of Information Science and Technology, Beijing University of Technology, Beijing, China; [3]Department of Otolaryngology, Head and Neck Surgery, Beijing Friendship Hospital, Capital Medical University, Beijing, China

Contributions: (I) Conception and design: Y Huang, P Zhao; (II) Administrative support: Z Wang, P Zhao; (III) Provision of study materials or patients: R Tang, N Xu, J Xie; (IV) Collection and assembly of data: Z Yang, H Yin; (V) Data analysis and interpretation: K Liu, X Li; (VI) Manuscript writing: All authors; (VII) Final approval of manuscript: All authors.

Correspondence to: Hongxia Yin, PhD. Department of Radiology, Beijing Friendship Hospital, Capital Medical University, No. 95 Yong'an Road, Xicheng District, Beijing 100050, China. Email: 282496774@qq.com; Xiaoguang Li, PhD. School of Information Science and Technology, Beijing University of Technology, No. 100, Pingleyuan, Chaoyang District, Beijing 100124, China. Email: lxg@bjut.edu.cn; Zhenchang Wang, MD, PhD; Pengfei Zhao, MD, PhD. Department of Radiology, Beijing Friendship Hospital, Capital Medical University, No. 95 Yong'an Road, Xicheng District, Beijing 100050, China. Email: cjr.wzhch@vip.163.com; zhaopengf05@163.com.

Background: Meniere's disease (MD) is an ear-related vestibular disorder accompanied by vertigo, hearing loss, and tinnitus. The anatomical structure and spatial position of the semicircular canals are important for understanding vestibular function and disease; however, research on MD and the effect of anatomical changes in the semicircular canals is limited. This study explored the relationship between the spatial location of the semicircular canals and MD using ultra-high-resolution computed tomography (U-HRCT) and intelligent segmentation.

Methods: Isotropic U-HRCT images obtained from patients with MD and healthy controls (HCs) were retrospectively analyzed. We extracted the semicircular canal structures and extracted their skeleton. The plane of the skeleton of each semicircular canal was fitted separately. The mutual angles between the semicircular canals, and the angles between each semicircular canal and each plane of the coordinate system were measured.

Results: Among 45 MD-affected ears (MDAEs), 33 MD-healthy ears (MDHEs), and 45 HC ears, the angle between the superior and lateral semicircular canals (LSCs) and the angle between the superior and posterior semicircular canals (PSCs) were larger in the MDAE and MDHE groups than the HC group ($P<0.01$), while the angle between the posterior and LSCs was smaller in the MDAE group than the HC group ($P<0.001$). The angles between the superior and PSCs and coronal plane (CP) of the coordinate system were significantly smaller in the MDAE and MDHE groups than the HC group ($P<0.01$); however, the angles between the LSC and axial plane and CP were significantly larger in the MDAE and MDHE

^ ORCID: Yan Huang, 0009-0001-2298-3971; Ke Liu, 0009-0002-6950-0321; Ruowei Tang, 0000-0002-0747-6672; Ning Xu, 0000-0001-6330-873X; Jing Xie, 0000-0003-3618-3761; Zhenghan Yang, 0000-0003-3618-3761; Hongxia Yin, 0000-0003-2804-1253; Xiaoguang Li, 0000-0002-7307-6263; Zhenchang Wang, 0000-0001-8190-6469; Pengfei Zhao, 0000-0002-9210-6544.

groups than the HC group (P<0.001).

Conclusions: Spatial position changes in the semicircular canals may be the anatomical basis of MD.

Keywords: Meniere's disease (MD); ultra-high-resolution computed tomography (U-HRCT); semicircular canals; spatial position; intelligent segmentation

Submitted Jan 29, 2024. Accepted for publication Jun 27, 2024. Published online Jul 30, 2024.
doi: 10.21037/qims-24-196
View this article at: https://dx.doi.org/10.21037/qims-24-196

Introduction

Meniere's disease (MD) is an ear-related vestibular disorder accompanied by clinical symptoms, including vertigo, hearing loss, and tinnitus (1,2). Its prevalence is approximately 50–200 per 100,000 adults, with a female-to-male ratio of 1:1.89, and a peak incidence between 20 and 60 years of age (3). Hallpike and Cairns first described endolymphatic hydrops (EH) as a characteristic pathological change in MD (4). The causes of EH in MD include anatomical changes of the temporal bone, genetics, and autoimmunity (5,6). The important aspects of MD include anatomical changes in the temporal bone, including poorly displayed vestibular aqueducts (7), the reduced width of vestibular aqueducts (8), and increased rates of jugular vein anomalies (9).

The anatomical structure and spatial position of the semicircular canals are important for studying vestibular function and disease. Traditional theory assumes that the ipsilateral semicircular canals are perpendicular to each other; however, they are not completely vertical or planar and demonstrate large changes in spatial position (10,11). By reviewing previous studies we found that research on the effect of anatomical changes in the spatial position of the semicircular canals on the onset of MD is lacking.

Computed tomography (CT) allows for the study of semicircular canals and their geometric shapes, and their three-dimensional (3D) reconstruction in living humans. In 1988, Takagi *et al.* undertook the computer-aided 3D reconstruction of human temporal bones (12). The in-plane spatial resolution of conventional multi-slice CT devices varies, and typically ranges between 0.23 and 0.35 mm (13,14). However, this is insufficient to visualize very small structures and occult lesions in the inner ear. The conventional reconstructed voxel size for the ultra-high-resolution CT (U-HRCT) developed in previous studies is 0.1 mm × 0.1 mm × 0.1 mm (15,16), and the smaller reconstructed voxel size is 0.05 mm × 0.05 mm × 0.05 mm (17), enabling the clear visualization of the bony anatomical structures of the ear.

Different methods are currently used to measure semicircular canal angles based on clinical CT images, with differing point positions and numbers, and mainly include the rotating coordinate plane and three-point plane equation methods (18). Most of these methods require manual segmentation and measurement. Due to the complex and irregular structure of the semicircular canal and large image changes, skilled operators are needed to perform manual segmentation. In the early stage, performing automatic segmentation of the inner ear quickly and accurately is possible through the segmentation network "sub-labyrinth net", which has good repeatability; with a segmentation time of approximately 10 s per side, it significantly improves clinical workflow efficiency (19,20).

In the present study, we applied this automated segmentation network to segment the three semicircular canals using U-HRCT data to explore the spatial position of the semicircular canals in patients with MD and investigate the anatomical factors in MD. We present this article in accordance with the STROBE reporting checklist (available at https://qims.amegroups.com/article/view/10.21037/qims-24-196/rc).

Methods

Patients

The study was conducted in accordance with the Declaration of Helsinki (as revised in 2013). The study was approved by the Ethics Committee of Beijing Friendship Hospital, affiliated with Capital Medical University (approval No. 2022-P2-259-02), and the requirement of individual consent for this retrospective analysis was waived.

We retrospectively collected data from 43 patients with MD who visited Beijing Friendship Hospital between June 2021 and March 2023. To be eligible for inclusion in this

study, the patients had to meet the following inclusion criteria: (I) have a definite diagnosis of MD based on the 2015 diagnostic criteria (21); and (II) have U-HRCT data available. Patients were excluded from the study if they met any of the following exclusion criteria: (I) had poor-quality CT images; (II) had inner ear malformations; and/or (III) had a history of ear surgery for MD. Qualitative distinction was used to exclude poor-quality CT images, including those with artifacts in the image and incomplete scan coverage. Subjects with normal ears were included as healthy controls (HCs) at a 1:1 ratio.

CT scan parameters and image analysis

CT scans were performed using a U-HRCT instrument (LargeV Instrument Corp., Beijing, China) with each patient in the supine position. The scan area covered the arcuate eminence of the stylomastoid foramen. Each patient was asked to relax and lie flat on the CT machine, and the bed entry position was the same for each test. Once the patient's head entered the CT, the patient was asked to stare at a fixed point. The scan parameters were as follows: tube voltage: 100 kV; tube current: 3.5 mA; and reconstructed voxel size: 0.1 mm × 0.1 mm × 0.1 mm. The scanning time was 40 s, and the reconstructed field of view was 65 mm × 65 mm; the scanning layer thickness and interlayer spacing were 0.1 mm with 370 layers. For each scan, the inner ear region of interest (ROI) was a fixed size of 224×224×160 voxels.

Segmentation

The automatic calibration did not require preprocessing; rather, the binarized lateral semicircular canal (LSC) obtained through segmentation with the original image was simply rotated. *Figure 1* shows the network flowchart. A two-stage segmentation framework, from coarse to fine, was used to obtain the substructures of the labyrinth (i.e., the five parts of the inner ear labyrinth) in the temporal bone CT images. The medical image data were 3D, and the structure of the image, such as the semicircular canal, was fixed in its position in the temporal bone. The LSC is a rigid structure; thus, only convolutional neural networks were required to learn the mapping relationship of its local area for segmentation. The coarse segmentation network was first used to determine the coarse mask of the external semicircular canal in the temporal bone CT images. Conversely, the fine segmentation network focused on learning more suitable feature maps in the localization area to segment the desired structure more accurately.

The coarse segmentation was performed using the 3D deep supervised densely network (18). After determining the LSC position, the region block localization ROI was extracted. The fine segmentation stage used the sub-volume block of the inner ear determined in the coarse segmentation stage as the input in the temporal bone CT based on a previous study (19). In this previous study, 18 cases of labeled data were used as the labeled data pool for the training iteration, 72 cases of data were used as the unlabeled data pool, 31 cases were used as the validation set, and 38 cases were used as the test set. In each iteration, 18 samples were screened out from the unlabeled sample pool with a different data screening method. Subsequently, as the samples were marked by experts, they were added to the labeled sample pool, until the entire unlabeled sample pool was empty. Therefore, this experiment used a total of five training iterations.

Simultaneously, based on the segmentation stage, we achieved fast and accurate separation of different substructures of the inner ear vestibule, cochlea, and superior semicircular canal (SSC), LSC, and posterior semicircular canal (PSC) (*Figure 2A*) by fine-tuning the decoding and end-clustering method. The label of the substructures was generated with a skeleton analysis scheme. Using a density-based clustering approach, the vestibule segment was subdivided, allowing the automatic annotation of pseudo-labels. Based on the pseudo-labels, we trained a transformer U-shaped network to segment the substructures of the labyrinth.

Skeleton extraction

Binary image refinement was applied to the segmented semicircular canal to extract its skeleton (*Figure 2B*). The skeleton extraction algorithm employed was based on previous studies (22,23). This algorithm can refine a connected region to a one-pixel width for feature extraction and topology representation. The following process was adopted:

(I) The 3D images were converted into a binary image containing only the target and background images.
(II) Morphological dilation was used to expand all the connected areas in the image outward until they contacted each other.
(III) Morphological erosion was applied to shrink all the edges in the previously expanded image inward until they were connected to the skeleton.

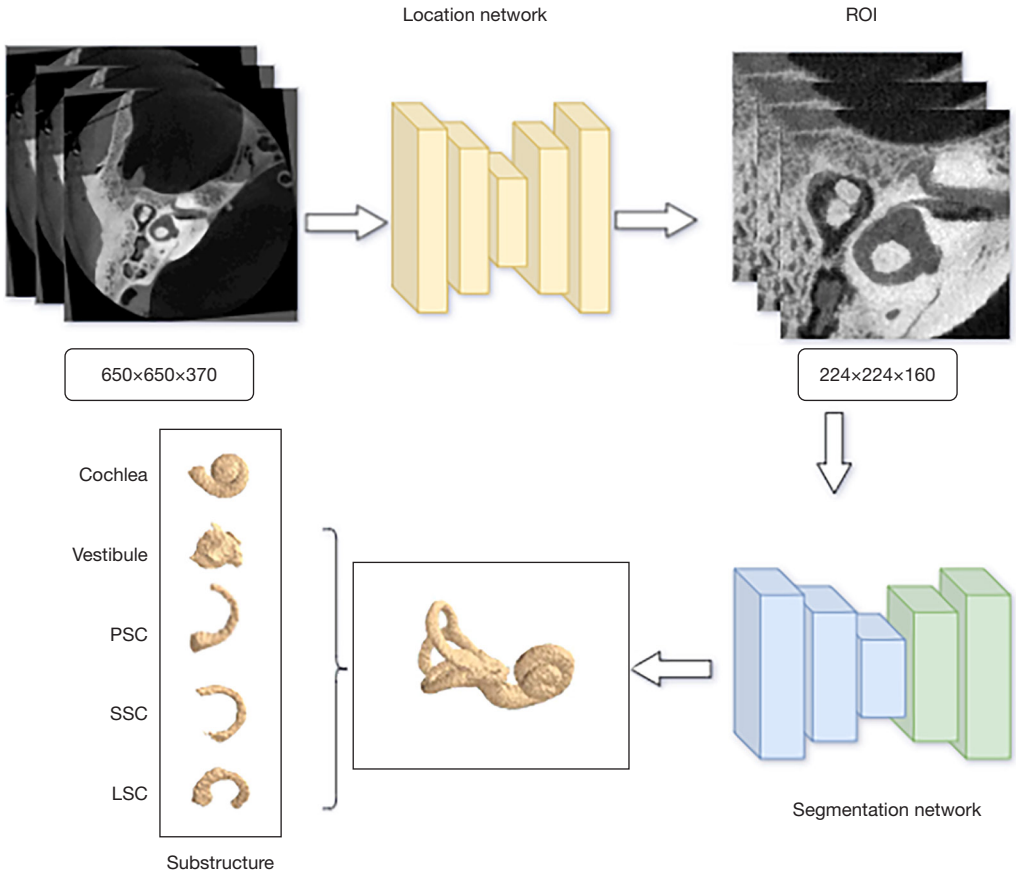

Figure 1 Network flowchart. The original slice size was 650 mm × 650 mm × 370 mm. After passing through the positioning network, we obtained the ROI of the inner ear region measuring 224×224×160 voxels. In the ROI, we obtained the inner ear segmentation structure through the segmentation network and fine-tuned the decoding end (green block) to obtain sub-structural segmentation. ROI, region of interest; PSC, posterior semicircular canal; SSC, superior semicircular canal; LSC, lateral semicircular canal.

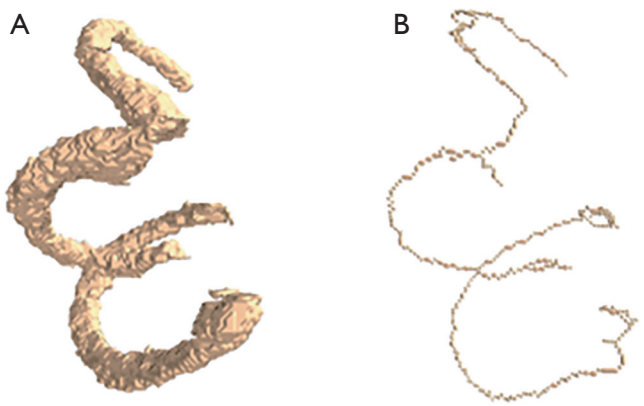

Figure 2 Three separated semicircular canals and their skeleton lines. From top to bottom, respectively, are the superior, lateral, and posterior semicircular canals. (A) The separated semicircular canals; and (B) the skeleton lines of the semicircular canals.

(IV) The eroded binary image was morphologically dilated to expand outward in all areas outside the skeleton.

(V) Steps 3 and 4 were repeated until the skeleton no longer changed. The formulas are expressed as follows:

$$S(A) = U_{k=0}^{K} S_k(A) \quad [1]$$

$$S_k(A) = (A \Theta kB) - (A \Theta kB) \circ B \quad [2]$$

where A represents the target image, B represents the structural elements, and the corrosion of A by B is denoted as $A \Theta B = \{z \mid Bz \subseteq A\}$, where k represents the number of operations performed.

During each morphological operation, the pixels in the image required updating. The values of all pixels connected

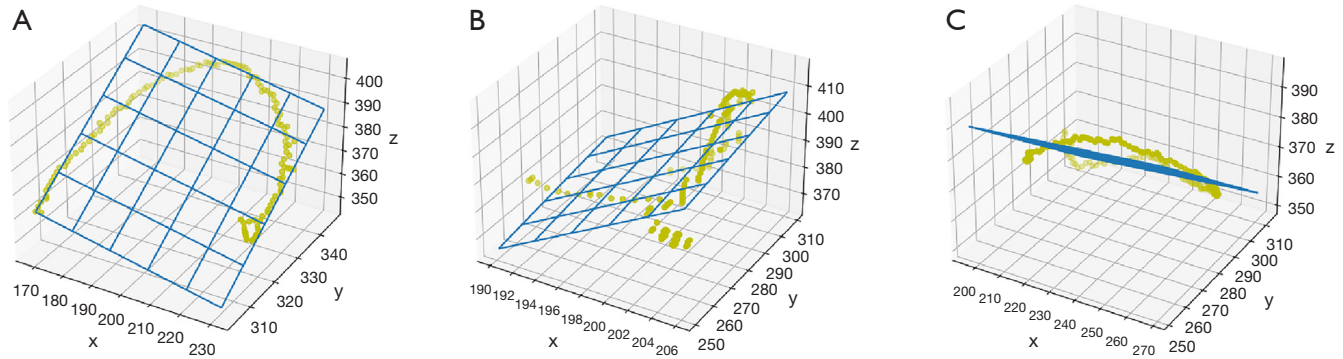

Figure 3 Fitting the semicircular canal plane using the least-squares method. (A) The superior semicircular canal plane; (B) the lateral semicircular canal plane; and (C) the posterior semicircular canal plane.

to the target pixel were set to the values of the target pixel through a dilation operation. Conversely, the values of all the pixels connected to the skeleton pixel were set to the values of the skeleton pixel through a corrosion operation. All the morphological operations were performed using the structural elements of a 3×3×3-sized cube. Repeated morphological expansion and corrosion operations provided a 3D extracted skeleton of three semicircular canals that was used to represent the target objects in the 3D image to analyze the internal structural features.

Measurement

The Digital Imaging and Communications in Medicine images of each participant's unilateral temporal bone using Python 3.7 (Python Software Foundation, USA) were illustrated within a 650 mm × 650 mm × 370 mm cube. Through this cube, the system could automatically generate a constructed coordinate system (Figure S1). Therefore, the coordinate system used in this study was the anatomical coordinate system. The sagittal plane (SP) is a vertical plane along the anterior and posterior diameters of the body, while the coronal plane (CP) is a vertical plane along the left and right diameters of the body perpendicular to the ground, and the axial plane (AP) is perpendicular to the longitudinal axis of the human body parallel to the ground. In this coordinate system, point cloud data from three semicircular tubes were obtained using the skeleton algorithm, and the three semicircular tubes were fitted to the plane using the least-squares method (*Figure 3*). For the semicircular canal data, we fitted a plane equation by minimizing the sum of the squares of the errors.

The matrix form of the least-squares method is expressed as follows:

$$Ax = b \quad [3]$$

where A is the matrix of $n \times k$, x is the column vector $k \times 1$, and b is the column vector $n \times 1$. When the vector x was made the smallest value for $\|Ax = b\|$, x was defined as the least-squares solution to the equation.

The normal vector of the fitted plane was determined using the fitted plane equation. By calculating the angle between the normal vectors, the mutual angle between the semicircular canals and the angle between the semicircular canals and the coordinate system plane were calculated separately (*Figure 4*).

Statistical analysis

We analyzed the data using SPSS 25.0 (IBM Corp., Armonk, NY, USA). The normally distributed quantitative variables are described as the mean and standard deviation (SD), while the non-normally distributed quantitative variables are described as the median (M) and interquartile boundary (P25, P75). The categorical variables are expressed as the frequency and percentage, n (%). An analysis of variance was used to compare the differences in spatial position among the three groups [i.e., MD-affected ears (MDAEs), MD-healthy ears (MDHEs), and HCs], and post-hoc pairwise comparisons were performed. For patients with bilateral MD, both ears were included in the MDAE group for the statistical analysis. Statistical significance was set at $P<0.05$. GraphPad Prism 9.0 (GraphPad Software, San Diego, California, USA) was used to display the overall data distribution among the three groups.

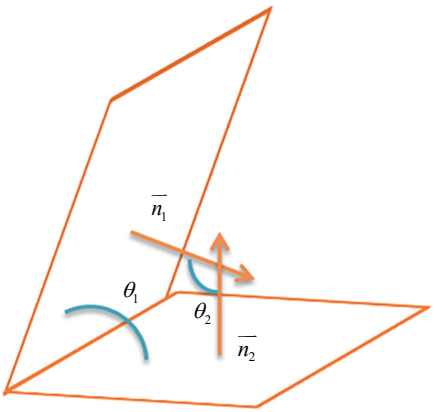

Figure 4 Determination of the mutual angles between the semicircular canals, and the angles between the semicircular canals and coordinate system plane. The planes are denoted as α and β, and $\overline{n_1}$ and $\overline{n_2}$ are their plane normal vectors. The angles between planes α and β, and between $\overline{n_1}$ and $\overline{n_2}$ are denoted as θ_1 and as θ_2, respectively. It can be concluded that $\theta_1=\theta_2$. Therefore, $\cos\theta=\cos\langle n_1|n_2\rangle=\frac{|n_1n_2|}{|n_1||n_1|}$.

Table 1 Demographic characteristics of patients with Meniere's disease

Clinical characteristics	Patients
Age (years)	57.41±13.45
Sex	
Male	15 (38.46)
Female	24 (61.54)
Lateral	
Unilateral	33 (84.62)
Bilateral	6 (15.38)

Data are expressed as the mean ± standard deviation or n (%).

Results

Study population

A total of 39 patients with MD [24 females, mean age: 57.41±13.45 years (range, 22–77 years)] were enrolled in this study. Among them, 33 patients had unilateral MD, and 6 had bilateral MD. Thus, a total of 45 ears were affected by MD, and 33 ears were healthy (*Table 1*). The HC group included 45 ears.

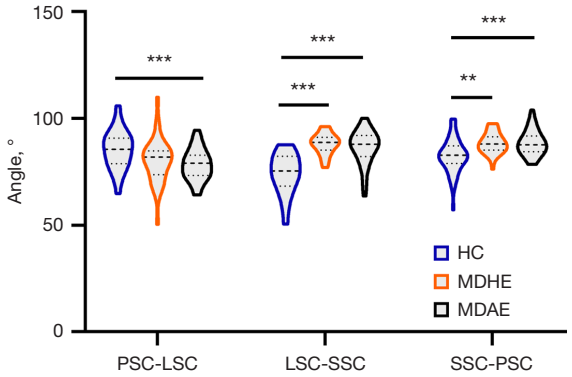

Figure 5 Comparison of the mutual angles of the semicircular canals among the MDHE, MDAE, and HC groups. **, P<0.01; ***, P<0.001. PSC, posterior semicircular canal; LSC, lateral semicircular canal; SSC, superior semicircular canal; HC, healthy control; MDHE, Meniere's disease-healthy ear; MDAE, Meniere's disease-affected ear.

Comparison of the mutual angles of the semicircular canals

The range of mean R^2 values for the different semicircular canals fit between the three groups was 0.58–0.78 (Table S1). *Figure 5* shows the angles between the three semicircular canals in the analyzed groups. We observed group differences in the angles between the PSC and LSC [F (2, 119) =7.924, P=0.001], and multiple comparison tests confirmed that this angle was significantly larger in the HC group than the MDAE group (P<0.001). The angles between the LSC and SSC and that between the SSC and PSC also differed among the groups [F (2, 113) =36.491, P<0.001 and F (2, 118) =10.629, P<0.001]. Specifically, the angles were significantly larger in the MDHE and MDAE groups than the HC group (all P<0.001) (*Table 2*).

Comparison of the angles between the semicircular canals and the planes of the 3D coordinate system

Figure 6A presents the results of the comparison of the angles between the LSC and planes in the 3D coordinate system among the three groups. We observed group differences in the angle between the LSC and the AP [F (2, 121) =21.659, P<0.001], as well as the angle between the LSC and the CP [F (2, 121) =46.324, P<0.001]. Post-hoc analyses indicated that both angles were significantly larger in the MDAE and MDHE groups than the HC group (all P<0.001).

Table 2 Group differences in the semicircular canal angles among the MDHE, MDAE, and HC groups

Variables	MDHE (n=33)	MDAE (n=45)	HC (n=45)	F-value	P value
PSC-LSC	80.18±10.51	77.52±9.21†***	85.40±8.90	7.924	0.001
LSC-SSC	88.21±5.03†***	86.50±7.90†***	74.16±9.30	36.491	<0.001
SSC-PSC	88.59±5.00†**	89.49±8.80†***	82.45±8.13	10.629	<0.001

Data are presented as the mean ± standard deviation. Significant after Bonferroni correction: **, P<0.01; ***, P<0.001; †, significantly different from HC. MDHE, Meniere's disease-healthy ear; MDAE, Meniere's disease-affected ear; HC, healthy control; PSC, posterior semicircular canal; LSC, lateral semicircular canal; SSC, superior semicircular canal.

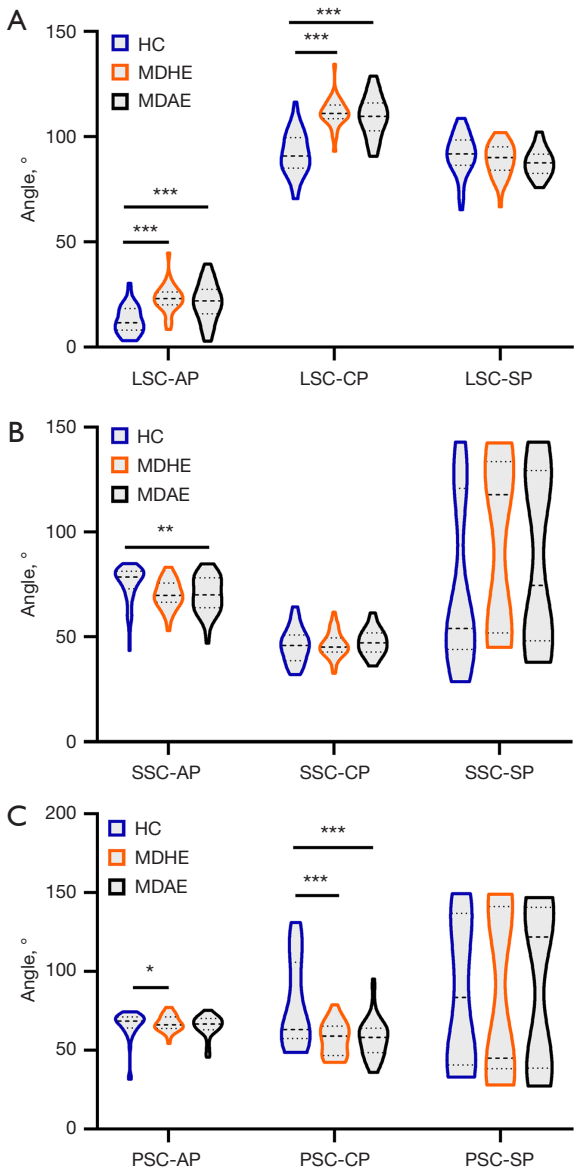

Figure 6 Comparison of the angles between the semicircular canal and planes of the three-dimensional coordinate system among the MDHE, MDAE, and HC groups. (A) Comparison of the angles between the lateral semicircular canal and planes in the 3D coordinate system among the three groups; (B) comparison of the angles between the superior semicircular canal and planes in the 3D coordinate system among the three groups; (C) comparison of the angles between the superior semicircular canal and planes in the 3D coordinate system among the three groups. *, P<0.05; **, P<0.01; ***, P<0.001. LSC, lateral semicircular canal; AP, axial plane; CP, coronal plane; SP, sagittal plane; SSC, superior semicircular canal; PSC, posterior semicircular canal; HC, healthy control; MDHE, Meniere's disease-healthy ear; MDAE, Meniere's disease-affected ear; 3D, three dimensional.

The results of the comparison of the angles between the SSC and planes in the 3D coordinate system among the groups are shown in *Figure 6B*. We found that the angles between the SSC and the AP were significantly larger in the HC group than the MDAE group [F (2, 121) =5.120, P=0.007]. However, the angle between the SSC and the CP did not differ significantly among the groups [F (2, 121) =0.729, P>0.05].

Figure 6C shows the results of the comparison of the angles between the PSC and planes in the 3D coordinate system among the analyzed groups. Group differences in the angle between the PSC and the AP were observed [F (2, 121) =4.883, P=0.009], such that the angle was significantly larger in the MDHE group than the HC group (P<0.05). In addition, the angle between the PSC and the CP also differed significantly among the groups [F (2, 121) =13.701, P<0.001], such that the angles were significantly smaller in the MDHE and MDAE groups than the HC group. All the statistical results described above are set out in *Table 3*.

Discussion

Principal results

This study applied 0.1-mm slice thickness U-HRCT to

Table 3 Group differences in the angles between the semicircular canal and planes of the three-dimensional coordinate system among the MDHE, MDAE, and HC groups

Variables	MDHE (n=33)	MDAE (n=45)	HC (n=45)	F-value	P value
LSC-AP	24.21±9.81†***	21.29±9.13†***	12.35±5.57	21.659	<0.001
LSC-CP	109.97±10.57†***	109.76±9.62†***	91.89±9.92	46.324	<0.001
LSC-SP	90.63±12.20	87.63±6.61	91.69±4.48	2.230	0.112
SSC-AP	70.23±6.61	67.44±15.85†**	75.18±9.17	5.120	0.007
SSC-CP	46.36±6.07	49.49±11.01	48.10±8.16	1.979	0.143
SSC-SP	94.64±39.87	87.43±39.77	73.04±38.04	3.153	0.056
PSC-AP	67.15±4.94†*	64.73±8.95	57.74±21.18	4.883	0.009
PSC-CP	57.12±10.32†***	60.47±19.07†***	79.40±27.58	13.701	<0.001
PSC-SP	85.25±52.52	91.78±49.55	84.25±44.83	0.312	0.733

Data are presented as the mean ± standard deviation. Significant after Bonferroni correction: *, P<0.05; **, P<0.01; ***, P<0.001; †, significantly different from HC. MDHE, Meniere's disease-healthy ear; MDAE, Meniere's disease-affected ear; HC, healthy control; LSC, lateral semicircular canal; AP, axial plane; CP, coronal plane; SP, sagittal plane; SSC, superior semicircular canal; PSC, posterior semicircular canal.

segment and measure the mutual angles of the semicircular canals and the angles between the semicircular canals and the coordinate system in patients with MD. The different spatial positions of the semicircular canals between patients with and without MD may indicate that congenital anatomical abnormalities in patients with MD can lead to disrupted endolymph production and circulation, resulting in EH. Conversely, the spatial position of the semicircular canals did not differ between the healthy and affected ears of patients with MD, which suggests that unilateral MD may eventually progress to become bilateral MD.

Comparison with previous findings

Traditionally, manual measurements of CT or magnetic resonance imaging (MRI) have been used to study the semicircular canal structure (11,24). Insufficient HRCT resolution may cause unclear boundary localization, which may affect accuracy. U-HRCT can more accurately extract semi-tubular contours and delineate centerlines. Due to their complex and irregular structure, semicircular canal images vary greatly; thus, operators must fully understand the characteristics of inner ear images. Moreover, calibration should be performed manually; for example, radiologists usually have to manually reconstruct the temporal bone CT slices to ensure that the bilateral anatomies are symmetrical, making the process time consuming, laborious, and prone to error. In addition, reconstruction software may be restricted, patented, or copyright protected, thus limiting its application. Moreover, the use of different standards prevents direct comparisons of the results.

In recent years, the application of deep learning in the field of medicine has been growing rapidly, helping clinicians to quickly and accurately segment target organs using CT images (25,26). We used deep learning to build an intelligent segmentation net and performed binary image thinning on segmented semicircular canal images to extract the skeletons of the semicircular canals. We then applied the least-squares method to fit the plane of each semicircular canal skeleton separately and to measure the mutual angles of the semicircular canals, and the angles between the semicircular canals and the coordinate system plane. This convenient, fast, and automated system is a useful clinical tool. In future studies, for conventional spiral CT, we will consider applying 3D rendering. Understanding the spatial angles of the semicircular canals of patients with MD can provide additional clinical information.

The semicircular canals can adapt to different directions and speeds of motion, thereby ensuring the stability and coordination of the body (27). The semicircular canals sense angular acceleration, and structural abnormalities may cause spatial orientation disorders (28). Compared with unaffected individuals, patients with MD have significantly higher cognitive failure questionnaire scores, which may be accompanied by corresponding cognitive impairments (29). The cognitive impairments caused by vertigo are often

dominated by visuospatial impairments (30,31).

Contradicting previous theories, our measurements revealed that the angles of the semicircular canals were not perfectly perpendicular in either the normal population or in patients with MD. Kim *et al.* (32) reported average angles between the anterior and horizontal semicircular canal planes, the horizontal and PSC planes, and the anterior and PSC planes of 83.7°, 82.5°, and 88.4°, respectively. Lyu *et al.* (33) observed that the angle between the anterior and PSC planes was >100°. Our results also showed that the mutual angles of the three semicircular canal planes were not perpendicular to each other, possibly because the semicircular canals themselves are not a regular circular shape. Moreover, the measurements of the mutual angles depend on the method used to fit the semicircular canal planes. The orthogonality deviates significantly between the semicircular canals in most species (24). In addition, we observed differences in the angle between the semicircular canal and the coordinate plane in MD. Considering that each study coordinate system is not exactly the same, this result requires a larger sample size for further validation.

Head rotation causes the endolymph in the semicircular canal to move in the opposite direction due to inertia, stimulating hair cells on the crista ampullaris. These cells transmit signals to the brain through the vestibular nerve, causing corresponding reflex actions to regulate muscle tension and eye movement (34,35). The significant difference in the spatial structure of the semicircular canals between patients with and without MD may lead to weakened self-regulation of motion, weakened vestibulo-ocular reflex, and higher sensitivity to vertigo in patients with MD. The abnormal spatial position of the semicircular canals may also affect endolymph flow or absorption, leading to changes in endolymphatic pressure and volume, which may cause MD symptoms. Our results showed the effect of spatial positional changes in the semicircular canals on MD; however, these anatomical factors may be a risk or triggering factor for MD, and there is no conclusive evidence that these factors have a direct causal relationship with the occurrence of MD. The etiology of MD may involve a combination of factors.

MD usually affects only one ear, and it is not yet clear whether unilateral MD will develop in the other ear. Due to differences in diagnostic criteria, examination methods, sample size, and regional differences, the true incidence of bilateral MD remains unknown (36). Approximately 14% of patients with unilateral MD progress to bilateral MD within an average of 7.6 years (37). In 1990, Yazawa *et al.* (38) performed a histological examination of the temporal bones in MD. Among 67 cases with EH, 20 (29.9%) showed bilateral EH. Morimoto *et al.* (39) reported EH in 29 unilaterally affected ears of patients with definite MD but not in the cochlea or the vestibule of eight of 29 non-affected ears. Pyykkö *et al.* (40) reported that approximately 90% of patients with MD had EH on gadolinium-enhanced MRI and that 75% of patients with unilateral symptoms of MD had bilateral hydrops.

We observed no significant difference in the spatial positions of the semicircular canals between the affected and healthy sides of MD in this study; however, the spatial positions of both ears of patients with MD differed from those of the normal population in the spatial position of the semicircular canals, further showing that while the healthy ear of MD patients may display no clinical symptoms of hearing loss or ear fullness, bilateral onset may occur. No effective methods exist to prevent or stop unilateral MD; however, the spatial position information of the semicircular canals can be used to non-invasively determine the risk of developing MD in the asymptomatic ear. After obtaining information on the spatial position of semicircular canals in patients with MD, pharmacotherapy, surgery, rehabilitation, and other methods can be used to control the frequency of vertigo attacks, preserve hearing and balance, and improve the quality of life of patients.

Limitations

This study had several limitations. First, the sample size was limited; therefore, future studies with more cases need to be conducted to gather further evidence to support our results. Second, the construction of this cubic coordinate system was based on anatomical coordinates, after instructing all patients to focus on a fixed point to ensure that both eye orbits were parallel to the horizontal plane of the coordinate system. However, even though all patients were in the same position during CT acquisition, the position of the semicircular canal may have varied somewhat. Further validation is needed using high-resolution CT with a larger field of view. Finally, we focused only on the spatial position of the semicircular canals and not that of the entire inner ear, such as the cochlea and vestibule. The spatial information of these structures will be measured during follow up to improve knowledge of the spatial anatomy of the inner ear of patients with MD.

Conclusions

Our results revealed significant differences in the spatial positions of the semicircular canals between patients with MD and HCs based on the application of intelligent segmentation and U-HRCT. These findings indicate that spatial position changes in the semicircular canals may be the anatomical basis of MD. This study is a preliminary research and exploratory work; hence, future larger-scale studies are needed to validate these findings and measure the spatial position of the entire inner ear, including the cochlea and vestibule.

Acknowledgments

Funding: This work was supported by the National Natural Science Foundation of China (Grant Nos. 62276012, 61931013, and 82171886), the Natural Science Foundation of Beijing Municipality (Grant No. 7222301), the Beijing Key Clinical Discipline Funding (Grant No. 2021-135), Beijing Scholar 2015 (Grant No. [2015]160), and Capital's Funds for Health Improvement and Research (Grant No. 2022-1-1111).

Footnote

Reporting Checklist: The authors have completed the STROBE reporting checklist. Available at https://qims.amegroups.com/article/view/10.21037/qims-24-196/rc

Conflicts of Interest: All authors have completed the ICMJE uniform disclosure form (available at https://qims.amegroups.com/article/view/10.21037/qims-24-196/coif). The authors have no conflicts of interest to declare.

Ethical Statement: The authors are accountable for all aspects of the work, including ensuring that any questions related to the accuracy or integrity of any part of the work have been appropriately investigated and resolved. The study was conducted in accordance with the Declaration of Helsinki (as revised in 2013). The study was approved by the Ethics Committee of Beijing Friendship Hospital, affiliated with Capital Medical University (approval No. 2022-P2-259-02), and the requirement of individual consent for this retrospective analysis was waived.

References

1. Gibson WPR. Meniere's Disease. Adv Otorhinolaryngol 2019;82:77-86.
2. Hoskin JL. Ménière's disease: new guidelines, subtypes, imaging, and more. Curr Opin Neurol 2022;35:90-7.
3. Basura GJ, Adams ME, Monfared A, Schwartz SR, Antonelli PJ, Burkard R, et al. Clinical Practice Guideline: Ménière's Disease. Otolaryngol Head Neck Surg 2020;162:S1-S55.
4. Hallpike CS, Cairns H. Observations on the Pathology of Ménière's Syndrome: (Section of Otology). Proc R Soc Med 1938;31:1317-36.
5. Sajjadi H, Paparella MM. Meniere's disease. Lancet 2008;372:406-14.
6. Nakashima T, Pyykkö I, Arroll MA, Casselbrant ML, Foster CA, Manzoor NF, Megerian CA, Naganawa S, Young YH. Meniere's disease. Nat Rev Dis Primers 2016;2:16028.
7. Mainnemarre J, Hautefort C, Toupet M, Guichard JP, Houdart E, Attyé A, Eliezer M. The vestibular aqueduct ossification on temporal bone CT: an old sign revisited to rule out the presence of endolymphatic hydrops in Menière's disease patients. Eur Radiol 2020;30:6331-8.
8. Grosser D, Willenborg K, Dellani P, Avallone E, Götz F, Böthig D, Warnecke A, Lanfermann H, Lenarz T, Giesemann A. Vestibular Aqueduct Size Correlates With the Degree of Cochlear Hydrops in Patients With and Without Menière's Disease. Otol Neurotol 2021;42:e1532-6.
9. Park JJ, Shen A, Keil S, Kuhl C, Westhofen M. Jugular bulb abnormalities in patients with Meniere's disease using high-resolution computed tomography. Eur Arch Otorhinolaryngol 2015;272:1879-84.
10. Cox PG, Jeffery N. Geometry of the semicircular canals and extraocular muscles in rodents, lagomorphs, felids and modern humans. J Anat 2008;213:583-96.
11. Suzuki K, Masukawa A, Aoki S, Arai Y, Ueno E. A new coordinates system for cranial organs using magnetic

resonance imaging. Acta Otolaryngol 2010;130:568-75.
12. Takagi A, Sando I. Computer-aided three-dimensional reconstruction and measurement of the vestibular end-organs. Otolaryngol Head Neck Surg 1988;98:195-202.
13. Yanagawa M, Tomiyama N, Honda O, Kikuyama A, Sumikawa H, Inoue A, Tobino K, Koyama M, Kudo M. Multidetector CT of the lung: image quality with garnet-based detectors. Radiology 2010;255:944-54.
14. Tsukagoshi S, Ota T, Fujii M, Kazama M, Okumura M, Johkoh T. Improvement of spatial resolution in the longitudinal direction for isotropic imaging in helical CT. Phys Med Biol 2007;52:791-801.
15. Tang R, Yin H, Wang Z, Zhang Z, Zhao L, Zhang P, Li J, Zhao P, Lv H, Zhang L, Yang Z, Wang Z. Stapes visualization by ultra-high resolution CT in cadaveric heads: A preliminary study. Eur J Radiol 2021;141:109786.
16. Tang R, Zhang Z, Zhao P, Zhao L, Xu N, Yin H, Yang Z, Wang Z. A novel imaging scoring method for identifying facial canal dehiscence: an ultra-high-resolution CT study. Eur Radiol 2023;33:2830-9.
17. Huang Y, Tang R, Xu N, Ding H, Pu W, Xie J, Yang Z, Liu Y, Gong S, Wang Z, Zhao P. Association Between Vestibular Aqueduct Morphology and Meniere's Disease. Laryngoscope 2024;134:3349-54.
18. Ancillao A. The helical axis of anatomical joints: calculation methods, literature review, and software implementation. Med Biol Eng Comput 2022;60:1815-25.
19. Li X, Gong Z, Yin H, Zhang H, Wang Z, Zhuo L. A 3D deep supervised densely network for small organs of human temporal bone segmentation in CT images. Neural Netw 2020;124:75-85.
20. Li X, Zhu Z, Yin H, Wang Z, Zhuo L, Zhou Y. Labyrinth net: A robust segmentation method for inner ear labyrinth in CT images. Comput Biol Med 2022;146:105630.
21. Lopez-Escamez JA, Carey J, Chung WH, Goebel JA, Magnusson M, Mandalà M, Newman-Toker DE, Strupp M, Suzuki M, Trabalzini F, Bisdorff A; Classification Committee of the Barany Society; Japan Society for Equilibrium Research; European Academy of Otology and Neurotology (EAONO); Equilibrium Committee of the American Academy of Otolaryngology-Head and Neck Surgery (AAO-HNS); Korean Balance Society. Diagnostic criteria for Menière's disease. J Vestib Res 2015;25:1-7.
22. Lee TC, Kashyap RL, Chu CN. Building skeleton models via 3-D medial surface axis thinning algorithms. Comput Vis Graph Image Process 1994;56:462-78.
23. Kollmannsberger P, Kerschnitzki M, Repp F, Wagermaier W, Weinkamer R, Fratzl P. The small world of osteocytes: connectomics of the lacuno-canalicular network in bone. New J Phys 2017;19:073019
24. Wimmer W, Anschuetz L, Weder S, Wagner F, Delingette H, Caversaccio M. Human bony labyrinth dataset: Co-registered CT and micro-CT images, surface models and anatomical landmarks. Data Brief 2019;27:104782.
25. Wu H, Liu J, Chen G, Liu W, Hao R, Liu L, Ni G, Liu Y, Zhang X, Zhang J. Automatic Semicircular Canal Segmentation of CT Volumes Using Improved 3D U-Net with Attention Mechanism. Comput Intell Neurosci 2021;2021:9654059.
26. Xu J, Liu J, Zhang D, Zhou Z, Jiang X, Zhang C, Chen X. Automatic mandible segmentation from CT image using 3D fully convolutional neural network based on DenseASPP and attention gates. Int J Comput Assist Radiol Surg 2021;16:1785-94.
27. Rabbitt RD. Semicircular canal biomechanics in health and disease. J Neurophysiol 2019;121:732-55.
28. Cheung B, Ercoline W. Semicircular Canal Size and Shape Influence on Disorientation. Aerosp Med Hum Perform 2018;89:744-8.
29. Rizk HG, Sharon JD, Lee JA, Thomas C, Nguyen SA, Meyer TA. Cross-Sectional Analysis of Cognitive Dysfunction in Patients With Vestibular Disorders. Ear Hear 2020;41:1020-7.
30. Bigelow RT, Agrawal Y. Vestibular involvement in cognition: Visuospatial ability, attention, executive function, and memory. J Vestib Res 2015;25:73-89.
31. Smith PF. The vestibular system and cognition. Curr Opin Neurol 2017;30:84-9.
32. Kim DK, Kim DR, Jeong SH, Kim GJ, Chang KH, Jun BC. Analysis of the coplanarity of functional pairs of semicircular canals using three-dimensional images reconstructed from temporal bone magnetic resonance imaging. J Laryngol Otol 2015;129:430-4.
33. Lyu HY, Chen KG, Yin DM, Hong J, Yang L, Zhang TY, Dai PD. The Age-Related Orientational Changes of Human Semicircular Canals. Clin Exp Otorhinolaryngol 2016;9:109-15.
34. Robinson DA. The functional operation of the vestibulo-ocular reflex. Prog Brain Res 2022;267:95-130.
35. Robinson DA. Basic framework of the vestibulo-ocular reflex. Prog Brain Res 2022;267:131-53.
36. Nabi S, Parnes LS. Bilateral Ménière's disease. Curr Opin Otolaryngol Head Neck Surg 2009;17:356-62.
37. House JW, Doherty JK, Fisher LM, Derebery MJ, Berliner KI. Meniere's disease: prevalence of contralateral ear involvement. Otol Neurotol 2006;27:355-61.

38. Yazawa Y, Kitahara M. Bilateral endolymphatic hydrops in Menière's disease: review of temporal bone autopsies. Ann Otol Rhinol Laryngol 1990;99:524-8.
39. Morimoto K, Yoshida T, Sugiura S, Kato M, Kato K, Teranishi M, Naganawa S, Nakashima T, Sone M. Endolymphatic hydrops in patients with unilateral and bilateral Meniere's disease. Acta Otolaryngol 2017;137:23-8.
40. Pyykkö I, Nakashima T, Yoshida T, Zou J, Naganawa S. Meniere's disease: a reappraisal supported by a variable latency of symptoms and the MRI visualisation of endolymphatic hydrops. BMJ Open 2013;3:e001555.

Cite this article as: Huang Y, Liu K, Tang R, Xu N, Xie J, Yang Z, Yin H, Li X, Wang Z, Zhao P. Spatial position changes in the semicircular canals may be the anatomical basis of Meniere's disease: a preliminary study based on ultra-high-resolution computed tomography (CT) and intelligent segmentation. Quant Imaging Med Surg 2024;14(8):6060-6071. doi: 10.21037/qims-24-196

